Supporting information

Interfacial engineering of $CuWO_4/WO_3$ thin films precisely fabricated by ultrasonic spray pyrolysis for improved solar water splitting

Feng Cao,[a] Yuhan Sun,[a] Xiaoyu Duan,[a] Mengyang Li,[a] Biao Chen,[a] Yang Cao,[a] Qinghua Liang,*[b] Amany M. El Nahrawy,[c] Gaowu Qin* [a]

a. Key Laboratory for Anisotropy and Texture of Materials (Ministry of Education), School of Material Science and Engineering, Northeastern University, Shenyang 110819, China.

b. Key Laboratory of Rare Earth, Ganjiang Innovation Academy, Chinese Academy of Sciences, Ganzhou, Jiangxi 341000, China.

c. Solid State Physics Department, Physics Research Division, National Research Centre,12622 El-Bohouth Str., Cairo, Egypt.

* Corresponding author.

E-mail addresses: qhliang@gia.cas.cn(Q. Liang), qingw@smm.neu.edu.cn (G. Qin)

Experimental Details

Materials

Copper nitrate trihydrate ($Cu(NO_3)_2 \cdot 3H_2O$), Ammonium metatungstate ($(NH_4)_6H_2W_{12}O_{40} \cdot XH_2O$) and other reagents of analytical grade were purchased from Sinopharm Chemical Reagent Co., Ltd. The aqueous solution was prepared with ultrapure water. The fluorine-doped tin oxide (FTO) glass was purchased from Dalian Qiseguang Solar Energy Technology Development Co., Ltd. The automated spray pyrolysis setup was purchased from Hangzhou Chifei Ultrasonic Equipment Co., Ltd.

Photoanodes preparation

In this experiment, WO_3, $CuWO_4$, and $CuWO_4/WO_3$ photoanode materials were fabricated by an automated spray pyrolysis setup (Fig. S1). The parameters of operating are as follows. The substrate temperature is 400 ℃. The air pressure is 0.001 MPa, and the speed for the constant flow pump is 1.0 mL min^{-1}. The distance from the nozzle to the heating table around 13.5 cm. The current for the electric box was kept at a mid-range value of 0.06 mA. The FTO glass with a size of 2.0 cm × 2.0 cm was alternatively cleaned by ultrasonic in acetone, ultra-pure water, and anhydrous ethanol for 30 min. Specifically, the aqueous solution of copper nitrate and ammonium metatungstate with a total concentration of 0.05 M was used as the reactant (200 mL). The atomic ratios of Cu and W are changed from 0:1, 1:1, 1:1.5, 1:2, and 1:2.5, respectively. The configured precursor solution was ultrasonic for 30 minutes to make the ions mix evenly. After heating the instrument substrate to 400 ℃, put the FTO glass on the substrate for preheating treatment (10 min). The spray time

was 15 min unless otherwise indicated (Start timing when fog drops appear). A further heating treatment at 550 °C for 2 h with a heating rate was 5 °C min^{-1} was carried out to improve the crystallinity after the film was deposited on FTO. The $CuWO_4/WO_3$ films with the ratio of $CuWO_4$ and WO_3 of 1:0.5, 1:1, and 1:1.5 were denoted as $CuWO_4/WO_3$-2.0, $CuWO_4/WO_3$-1, and $CuWO_4/WO_3$-0.67, respectively.

Characterization

The phase of the film was characterized by a Smartlab X-ray diffractometer (XRD, Nippon Science). The Cu target is used as the target material($K\alpha_1$=0.15405980), the working voltage is 40 kV, the working current is 200 mA, and the power is 18 kW. The step-by-step method is used to test the XRD of the sample. The test range is 10° ~ 90° and the scanning speed is 5°/min. The morphology observation was observed by a field emission scanning electron microscope (FESEM, JSM-7001F) and transmission electron microscope (TEM, JSM-2100F, JEOL). JSM-7001F is equipped with an energy dispersive X-ray (EDX) spectrometer to analyze the elemental composition of the film at a voltage of 15kV. The optical and adsorption properties were measured with a UV-Vis spectrophotometer with Labsphere integrating sphere (Lambda 750s, PerkinElmer). The test wavelength range of the sample is 350 nm ~ 800 nm, and the backplane is white $BaSO_4$. Further chemical analysis was performed using an X-ray photoelectron spectroscope (XPS) with an Al Kα radiation source (1486.6 eV). The specimen surfaces were sputtered with argon ions (2.0 kV) for depth profiling. The sputtering rate was ~30 nm/min, calculated using calibration done on a SiO_2 sample and correlating it to the steel sample (this routine was found to be reasonable by

comparing XPS depth profiles with SEM and TEM micrographs of cross-sections). Peak fitting of the XPS peaks was performed in the Casa XPS software package. The XPS data were calibrated for charge shift by normalizing binding energies to that of the adventitious C 1s peak at 284.8 eV. Determine the thickness of the sample with a step profiler (Dektak 150, Veeco). To ensure the accuracy of film thickness measurement, ten different positions were selected for each sample to measure the film thickness, and the average value was recorded as the thickness.

The optical band gap

To calculate valence band position, the optical band gap was determined by the following Tauc equation[1]:

$$(\alpha h\upsilon)^{1/2} = A(h\upsilon - E_g) \quad (1)$$

where α, h and υ are absorption coefficient, Planck's constant, and light frequency, respectively. A and E_g are constants and bandgap, respectively.

Photoelectrochemical (PEC) performance test

The PEC testing of photoanodes was carried out on the electrochemical workstation (Zahner IM6e, Germany). During the PEC testing, a xenon lamp (CHF-XM-500W) with a filter plate was used to simulate a solar light source with an output power of 100 mW cm^{-2} (AM 1.5 G). The procedure for preparing the working electrode is as follows: (1) The sample was cut into pieces of size 0.5 cm × 1.0 cm and then was trimmed about 10 cm of the copper core electrode wire. 1.0 cm of the insulation was stripped off at one end and 0.3 cm of that was stripped off at the other end of the wire. The stripped end of the electrode wire was fixed onto the surface of the sample; (2)

The sample was coated on the surface after sanding to remove the exposed FTO surface SnO_2 layer held by the clip. The silver paste was applied uniformly to bond the electrode wire and the sample after drying; (3) An equal amount of acrylic acid glue solution was extruded and used to fix the area around the electrode wire, leaving a certain area of the sample surface exposed; (4) The contact points between the wires and the sample was carefully sealed as well as around the sample to ensure good contact. The photoanode, Pt net, and Ag/AgCl (sat. KCl) were used as the working, counter, and reference electrodes, respectively. 0.5 M Na_2SO_4 (pH = 6.4) was explored as the electrolyte to establish a three-electrode system for PEC testing. Linear voltammetric scanning (LSV) was performed in a range of 0.57~1.67 V (vs Ag/AgCl) at 10 mV/s under dark and light states. The electrochemical impedance spectra (EIS) were conducted in the frequency range of 1×10^5~10^{-1} Hz with a DC bias of 1.23 V vs. Ag/AgCl. The Mott-Schottky test was carried out with a frequency of 1 kHz. The test data was converted to a reversible hydrogen electrode standard using the equation[2]:

$$E_{RHE} = E_0 + 0.059pH + E_{Ag/AgCl} \quad (2)$$

Where E_0 is the electrode potential obtained by experiment, $E_{Ag/AgCl}$ is 0.197 V at 25 °C in 0.5 M Na_2SO_4 electrolyte.

Mott–Schottky (M-S) plots

The charge carrier density (N_d) is calculated by the equation:

$$\frac{1}{C_{SC}^2} = \frac{2}{\varepsilon_0 \varepsilon_r N_D e}\left(E - E_{FB} - \frac{kT}{e}\right) \quad (3)$$

Where C_{SC}, N_D, ε_0, and ε_r represent the space charge capacitance, carrier concentration, vacuum dielectric constant, and the dielectric constant of the semiconductor, respectively. E and E_{FB} are the applied potential and flat charge potential, respectively. T is the temperature (298 K), and k refers to the Boltzmann constant. $1/C_{SC}^2$ represents the slope of the fitted M-S curve. Here, $\varepsilon_0 = 8.85 \times 10^{-14}$ $F \cdot cm^{-1}$, $k = 1.38 \times 10^{-23}$ J k^{-1}, and $e = 1.602 \times 10^{-19}$ C.

O_2 evolution experiment

O_2 evolution experiment was conducted at 1.23 V vs. RHE under AM1.5 illumination in 1M NaOH. The amounts of evaluated O_2 were measured via the Dissolved oxygen meters. It is worthwhile to note that the electrolyte should be bubbled with highly pure N_2 for 30 min to remove the dissolved oxygen before the measurement, and the cell should be carefully sealed.

Computational methods and models

The spin-polarized periodic density functional theory calculations were performed using the Vienna Ab-initio Simulation Package (VASP) code.[3] To improve the calculation efficiency, core electrons were replaced by the projector augmented wave (PAW) pseudo-potentials.[4] The generalized gradient approximation of the Perdew, Burke, and Ernzernhof (PBE) functional was utilized for the exchange and correlation.[5] It is well known that standard density functionals, such as the generalized gradient approximation (GGA) of Perdew, Burke and Ernzerhof (PBE), tend to underestimate band gaps. Instead, the hybrid density functional Heyd-Scuseria-Ernzerhof (HSE) is preferred for a more accurate calculation of the bandgap

than PBE. So, we adopted the HSE scheme to calculate the electronic band structures and density of states. The wave functions were expanded in plane waves with cut-off energy of 300 eV. The convergence criterion for the electronic self-consistent iteration was set to 10^{-4} eV, and the change of the total energy on each atom was less than 0.001 eV between two ionic steps. Brillouin zone integration was approximated by a sum over special k points ($3 \times 3 \times 1$) chosen using the Monkhorts-Pack meshes centered at the Γ point. To avoid interactions between periodic images, a vacuum layer of 20 Å is added to the adjacent slabs in both models.

First, we achieve the unit cell of WO_3 and $CuWO_4$ after the Geometry optimization. Then we optimized the slab of WO_3 and $CuWO_4$, selecting the (001) and (110) facets as the terminating surface of the slab. To build the WO_3-(001)/$CuWO_4$-(110) interface, WO_3-(001) is used to match the $CuWO_4$-(110) surface. $CuWO_4$ and WO_3 are triclinic and monoclinic cell, respectively. We then optimized the slab of WO_3 and $CuWO_4$, selecting the (001) and (110) facets as the terminating surface of the slab (Fig. S2 and S3). To build the WO_3-(001)/$CuWO_4$-(110) interface, 2×1 WO_3-(001) are used to match the $3 \times \sqrt{2}$ $CuWO_4$-(110) surface (Fig. S4). The lattice mismatch rate is 3.89%, which is within the allowable range of experimental synthesis.

After the interface structure was established, the stability of the interface structure was studied by analyzing the formation energy of the optimized structure. The energetic stability of WO_3/$CuWO_4$ interface was evaluated as[6]:

$$E_f = (E_{total} - E_{WO_3} - E_{CuWO_4})/N \quad (4)$$

Where E_f is the formation energy of the WO_3/$CuWO_4$, E_{total} is the total energy of

the $WO_3/CuWO_4$, E_{WO_3} and E_{CuWO_4} are the total energies of WO_3 and $CuWO_4$, respectively. N is the total number of atoms in the heterostructure.

The calculated formation energy of the $WO_3/CuWO_4$ is -98.84 eV/atom, suggesting that the formation of $WO_3/CuWO_4$ heterostructure is an exothermic process. This also indicates that the $WO_3/CuWO_4$ heterostructure can be synthesized experimentally.

In this work, using the slab model, the work function is computed with the equation[7]:

$$\Phi = \Delta\bar{V}_{vac\text{-}bulk} + \bar{V}_{bulk} - E_{BGC} \quad (5)$$

Where $\Delta\bar{V}_{vac\text{-}bulk}$ is the potential in the vacuum region relative to the average electrostatic bulk region of the slab. The slab should be sufficiently thick to mimic the bulk of the material, and the vacuum region should be large enough to avoid interaction with the neighboring replica. $\bar{V}_{bulk}$ is the bulk electrostatic potential averaged over the plane parallel to the specific surface of bulk semiconductors. E_{BGC} is the bandgap center position.

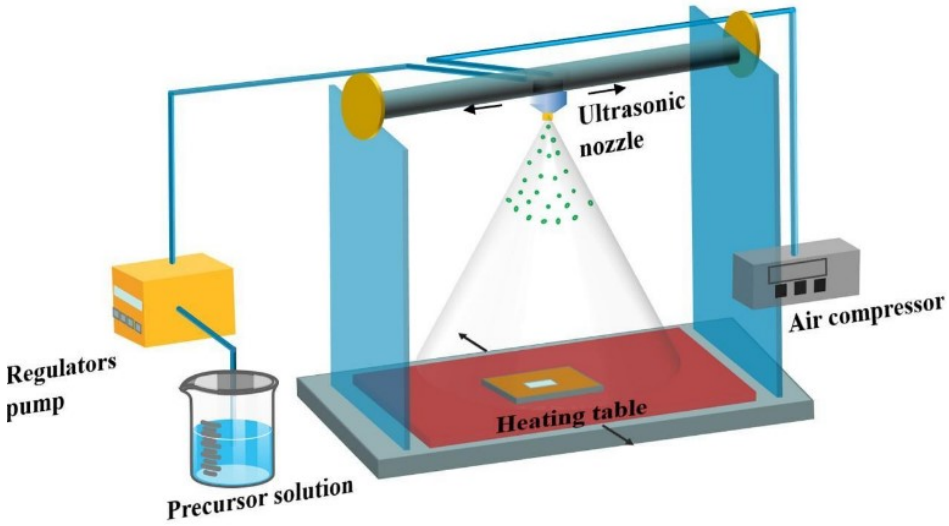

Fig. S1 Schematic diagram of automatic ultrasonic spray pyrolysis device.

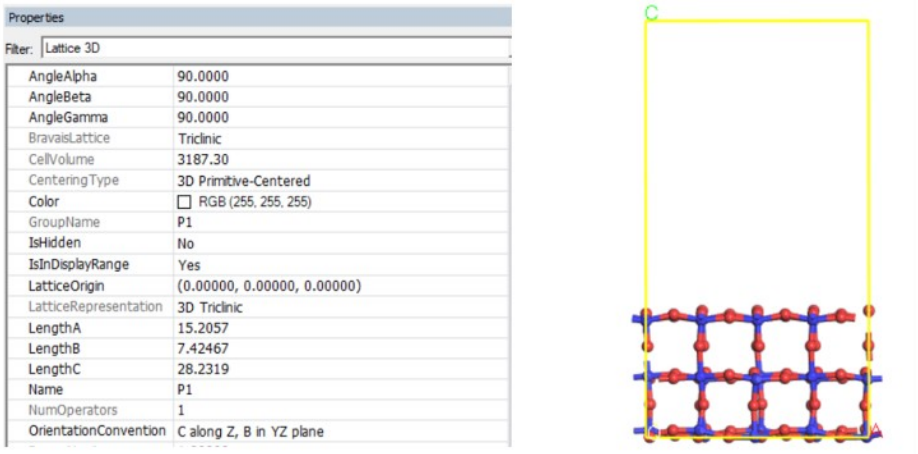

Fig. S2 Basic lattice parameters of WO_3.

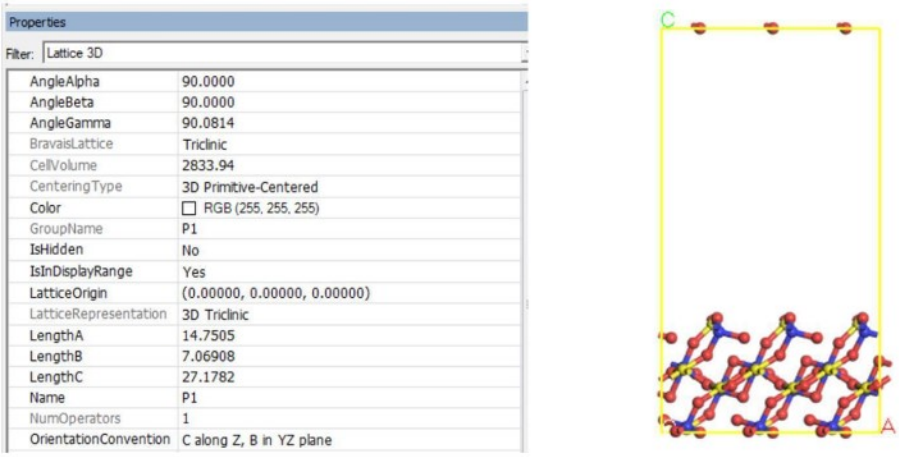

Fig. S3 Basic lattice parameters of $CuWO_4$.

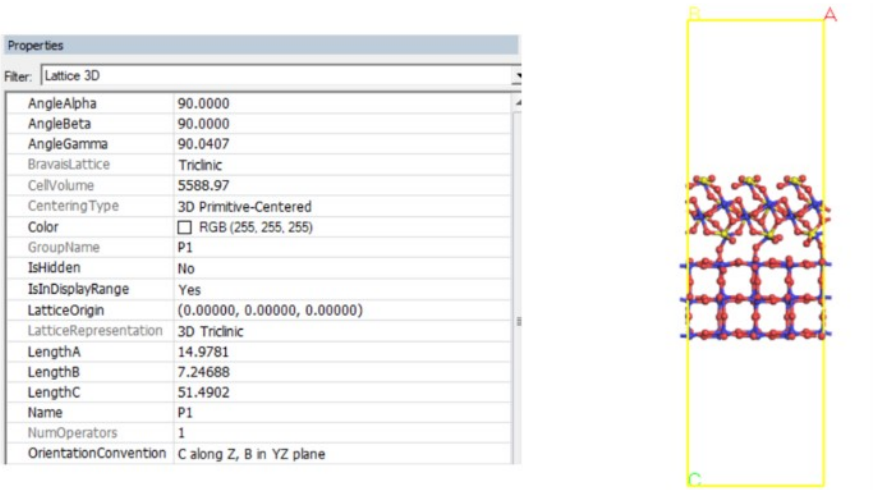

Fig. S4 Basic lattice parameters of $CuWO_4(110)/WO_3(001)$ heterostructure

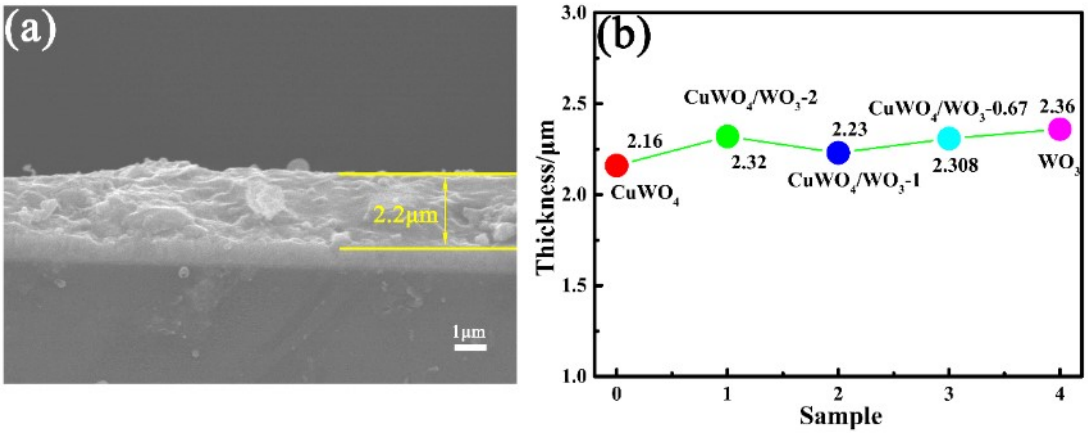

Fig. S5 The thickness of $CuWO_4/WO_3$ films. (a) The cross-sectional SEM image of the $CuWO_4/WO_3$-1 film. (b) The thickness of different $CuWO_4/WO_3$ films.

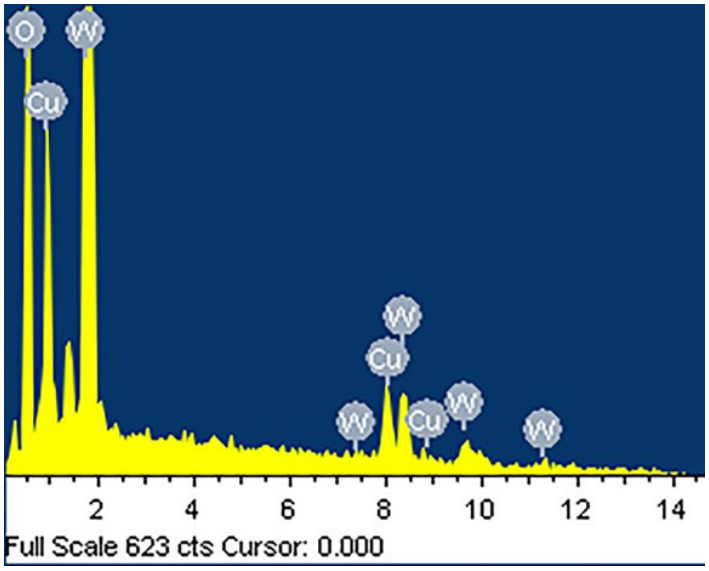

Fig. S6 EDS spectrum of the as-prepared $CuWO_4/WO_3$-1 film.

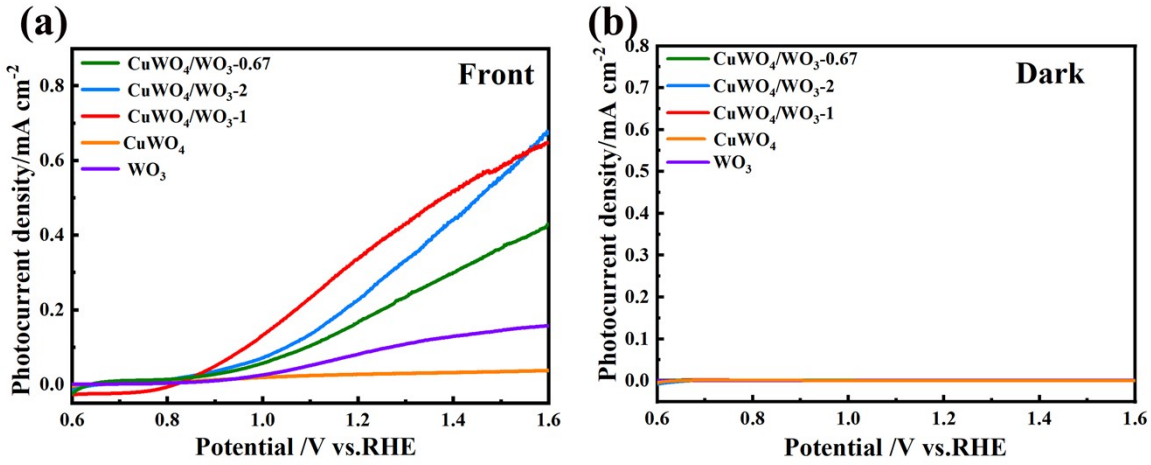

Fig. S7 LSV curves of different $CuWO_4/WO_3$ films under (a) front-side illumination and (b) dark state.

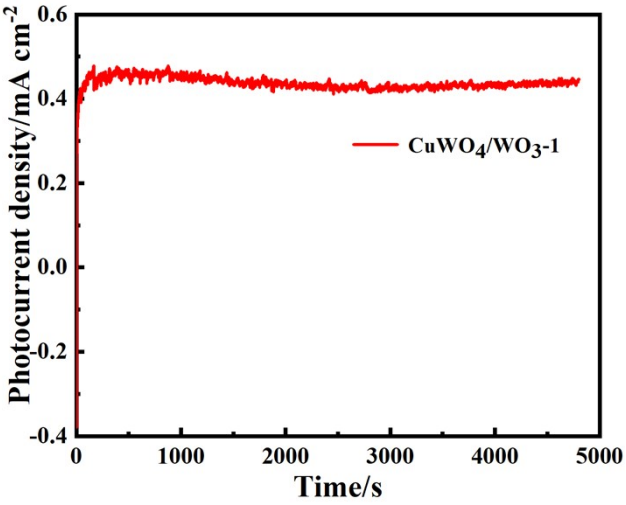

Fig. S8 The stability of $CuWO_4/WO_3$-1.

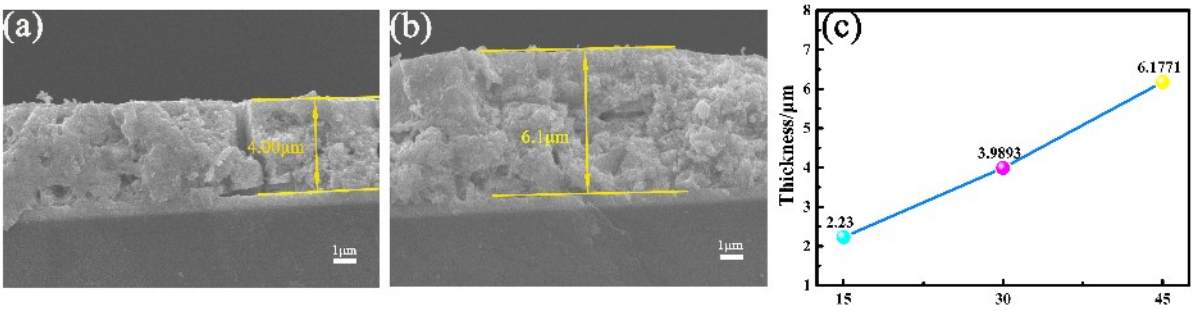

Fig. S9 (a-b) The cross-sectional SEM images of the $CuWO_4/WO_3$-1 films with spraying time of 30 min and 45 min respectively. (c) The thickness of $CuWO_4/WO_3$-1 film fabricated at different spraying time.

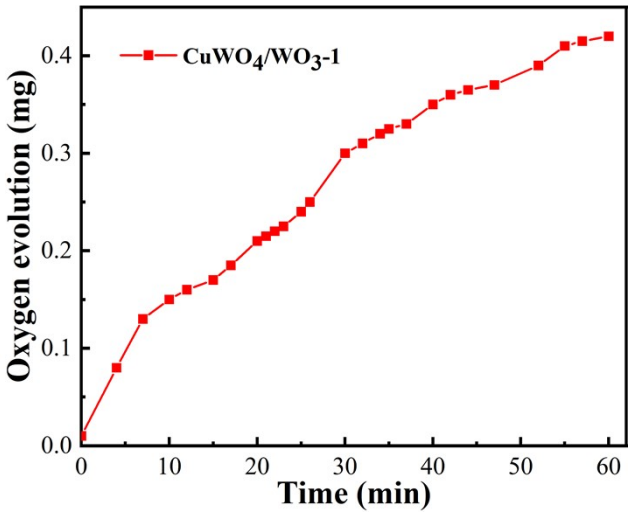

Fig. S10 The time course of O_2 evolution over the as-prepared $CuWO_4/WO_3$-1

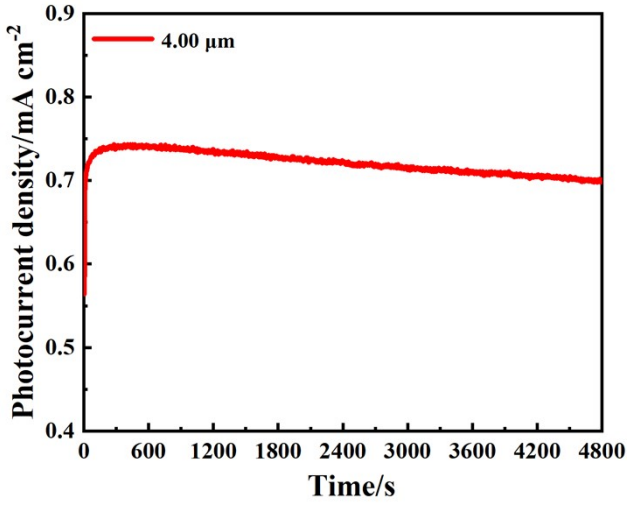

Fig. S11 The stability of $CuWO_4/WO_3$-1-4μm.

Table S1. The Bader charges of atoms (concerning the neutral atom) in WO_3 (001)/$CuWO_4$ (110) heterojunction.

$CuWO_4$ part			WO_3 part	
Cu	W	O	W	O
-0.84	-2.57	0.89	-2.45	0.89

Table S2. Calculation of chemical composition (Atomic content)% of $CuWO_4/WO_3$ and $CuWO_4$ films by EDS and XPS techniques.

Element	$CuWO_4$	$CuWO_4$	$CuWO_4/WO_3$-1	$CuWO_4/WO_3$-1
	EDS	XPS	EDS	XPS
O	66.88	67.54	70.19	68.22
Cu	15.89	16.97	9.25	9.86
W	17.24	15.49	20.56	21.92
Total	100	100	100	100
W:Cu(actual)	1.08:1	0.91:1	2.22:1	2.22:1
W:Cu(plan)	1:1	1:1	2:1	2:1

Table S3. The chemical composition (Atomic content)% for $CuWO_4/WO_3$ films.

Element	$CuWO_4$	$CuWO_4/WO_3$-2	$CuWO_4/WO_3$-1	$CuWO_4/WO_3$-0.67
O	66.88	66.91	70.19	67.87
Cu	15.89	13.06	9.25	8.32
W	17.24	20.03	20.56	23.81
Total	100	100	100	100
W:Cu(actual)	1.08:1	1.53:1	2.22:1	2.86:1
W:Cu(plan)	1:1	1.5:1	2:1	2.5:1

Table S4. The steady state current I_{st} for different $CuWO_4/WO_3$ composites.

	$CuWO_4$	WO_3	$CuWO_4/WO_3$-1	$CuWO_4/WO_3$-2	$CuWO_4/WO_3$-0.67
I (mA cm^{-2})	0.06613	0.02733	0.3718	0.213	0.203

Table S5. The calculated N_d (cm^{-3}) for different $CuWO_4/WO_3$ composites.

Sample	WO_3	$CuWO_4$	$CuWO_4/WO_3$-2	$CuWO_4/WO_3$-1	$CuWO_4/WO_3$-0.67
N_d	6.39×10^{19}	2.65×10^{18}	1.4×10^{20}	1.47×10^{20}	8.89×10^{19}

Table S6. The fitting resistance for the EIS curve of $CuWO_4/WO_3$ at 1.23 V vs.RHE

Samples	Fitted resistance /ohm	
	R2	R3
$CuWO_4$	1905	88126
$CuWO_4/WO_3$-2	191.1	14918
$CuWO_4/WO_3$-1	37.99	12781
$CuWO_4/WO_3$-0.67	204.6	15963
WO_3	2330	26671

Table S7. PEC water splitting performance of the $CuWO_4$-based photoanodes.

Materials(film)	Electrolyte	Onset potential	Photocurrent	Ref
$CuWO_4/WO_3$	**0.5 M $NaSO_4$**	**0.65 V_{RHE}**	**0.66 mA cm^{-2} at 1.23 V vs. RHE**	**This work**
$CuWO_4/WO_3$	0.2 M KPi	0.6 V_{RHE}	0.48 mA cm^{-2} at 1.23 V vs. RHE	[8]
WO_3@$CuWO_4$	0.1 M phosphate	———	0.4 mA cm^{-2} at 1.5 V vs. RHE	[9]
Ag-$CuWO_4/WO_3$	0.1 M phosphate	———	0.365 mA cm^{-2} at 1.23 V vs. RHE	[10]
$CuWO_4/WO_3$	0.5 M $NaSO_4$	———	0.45 mA cm^{-2} at 1.2 V vs. RHE	[11]
$CuWO_4/WO_3$	0.1 M KP_i	———	0.3 mA cm^{-2} at 1.23 V vs. RHE	[12]
$Co_3O_4/CuWO_4$	0.1 M KP_i	———	0.57 mA cm^{-2} at 1.23 V vs. RHE	[13]
$CuWO_4$/CoPi	0.1 M phosphate	———	0.371 mA cm^{-2} at 1.23 V vs. RHE	[14]
$CuW_{1-x}Mo_xO_4$	0.1 M phosphate	———	0.46 mA cm^{-2} at 1.23 V vs. RHE	[15]
$CuWO_4$	0.1 M phosphate	———	0.3 mA cm^{-2} at 1.23 V vs. RHE	[16]

References

1 Y. Zhu, J. Chen, L. Shao, X. Xia, Y. Liu, L. Wang, Appl. Catal. B Environ. 2020, 268, 118744.

2 S.S. Kalanur, R. Singh, H. Seo, Appl. Catal. B Environ. 2021, 295, 120269.

3 J. Hafner, J. Comput. Chem. 2008, 29, 2044-2078.

4 G. Kresse, J. Furthmüller, Comput. Mater. Sci. 1996, 6, 15-50.

5 J.P. Perdew, K. Burke, M. Ernzerhof, Phys. Rev. Lett. 1998, 80, 891.

6 N.E. Singh-Miller, N. Marzari, Phys. Rev. B. 2009, 80, 235407.

7 J. Beatty, T. Cheng, Y. Cao, M.S. Driver, W.A. Goddard III, J.A. Kelber, J. Phys. Chem. Lett. 2017, 8, 188-192.

8 T. Wang, X. Fan, B. Gao, C. Jiang, Y. Li, P. Li, S. Zhang, X. Huang, J. He, ChemElectroChem. 2021, 8, 125-134.

9 I. Rodríguez-Gutiérrez, E. Djatoubai, M. Rodríguez-Pérez, J. Su, G. Rodríguez-Gattorno, L. Vayssieres, G. Oskam, Electrochim. Acta. 2019, 308 , 317-327.

10 R. Salimi, A.A.S. Alvani, B.T. Mei, N. Naseri, S.F. Du, G. Mul, New J. Chem. 2019, 43, 2196-2203.

11 D. Wang, P.S. Bassi, H. Qi, X. Zhao, L.H. Wong, R. Xu, T. Sritharan, Z. Chen, Materials (Basel). 2016, 9, 348.

12 J.E. Yourey, J.B. Kurtz, B.M. Bartlett, J. Phys. Chem. C. 2012, 116, 3200-3205.

13 C.M. Tian, M. Jiang, D. Tang, L. Qiao, H.Y. Xiao, F.E. Oropeza, J.P. Hofmann, E.J.M. Hensen, A. Tadich, W. Li, J. Mater. Chem. A. 2019, 7, 11895-11907.

14 S. Chen, M.N. Hossain, A. Chen, ChemElectroChem. 2018, 5 , 523-530.

15 Q. Liang, Y. Guo, N. Zhang, Q. Qian, Y. Hu, J. Hu, Z. Li, Z. Zou, Sci. China Mater. 2018, 61, 1297-1304.

16 D. Hu, P. Diao, D. Xu, M. Xia, Y. Gu, Q. Wu, C. Li, S. Yang, Nanoscale. 2016, 8, 5892-5901.